www.sciencemag.org/content/350/6259/430/suppl/DC1

Supplementary Materials for

Reduced grid-cell–like representations in adults at genetic risk for Alzheimer's disease

Lukas Kunz, Tobias Navarro Schröder, Hweeling Lee, Christian Montag, Bernd Lachmann, Rayna Sariyska, Martin Reuter, Rüdiger Stirnberg, Tony Stöcker, Paul Christian Messing-Floeter, Juergen Fell, Christian F. Doeller, Nikolai Axmacher*

*Corresponding author. E-mail: nikolai.axmacher@rub.de

Published 23 October 2015, *Science* **350**, 430 (2015)
DOI: 10.1126/science.aac8128

This PDF file includes:

Materials and Methods

Participants and *APOE* genotyping

We recruited 531 healthy Caucasian participants in different lectures of the University of Bonn and performed genotyping by means of buccal swabs. Automatic purification of genomic DNA was conducted via the MagNA Pure® LC system using a commercial extraction kit (MagNA Pure LC DNA isolation kit; Roche Diagnostics, Mannheim, Germany). Analysis of the *APOE* polymorphisms was performed with real-time polymerase chain reaction (PCR) on a Light Cycler System by Roche. Primers and hybridization probes were provided by TIBMOLBIOL, Berlin, Germany. From this large cohort, we successively and randomly invited male and female participants (age range, 18 – 30 years) who were either homozygous for *APOE*-ε3 ("control participants") or heterozygous for *APOE*-ε4/ε3 ("risk participants") to the fMRI experiment until at least 20 participants were scanned in each of the four groups (male control, female control, male risk, and female risk). Sample sizes were based on Doeller et al. (*15*) and previous *APOE*-fMRI-studies (e.g., ref. *21*). No statistical method was used to predetermine sample size. We did not include a third genetic subgroup with homozygous *APOE*-ε4-carriers, because they were too rare ($n = 8$). Participants as well as experimenters were blinded towards genotypes. Participants' real names and genotypes were never directly connected. In total, 94 participants were scanned. Ten participants did not complete the experiment and 9 had to be excluded because of excessive head motion (more than 4 mm into one or more translational directions). Thus, all analyses were performed with a final number of $N = 75$ participants ($n = 18$ male control, $n = 19$ female control, $n = 18$ male risk, and $n = 20$ female risk). Control and risk groups did not differ in demographic characteristics (see Table S1). All participants had normal or corrected-to-normal vision and reported no history of neurological or psychiatric disease. The local Ethics Committee of the University of Bonn approved the study and all participants signed a written informed consent.

Experimental task

The paradigm was adapted from Doeller et al. (*15*). During the fMRI scan, participants performed an object-location memory task navigating freely in a circular virtual arena. The arena comprised a grassy plane (diameter of 9,500 virtual units) bounded by a cylindrical cliff. No intra-maze landmark (as used in previous versions of the task; *28*, *15*) was present. Movement in the arena was enabled using a button box with three buttons for the different movement directions (move forward, turn right, turn left) and one button for object placement. The total duration of 78 minutes was divided into 6 sessions of 13 minutes each. Sessions were separated by short breaks. At the very beginning of session 1, participants collected eight everyday objects (randomly drawn from a total number of 12 potential objects: eggplant, baby bottle, briefcase, globe, bucket, rubber duck, barrel, stapler, agenda, vase, alarm clock, basketball) from different locations in the arena ("initial learning phase"). This time period (variable duration of approximately two minutes, as the whole task was self-paced) was excluded from all analyses by removing the corresponding fMRI volumes. Object locations were randomly distributed and similarly central between the two genetic subgroups (measured as the mean distance between the object locations and the arena center; two-sample *t*-test, $t_{73} = -$

.617, P = .539). Several constraints ensured that the object positions were not too close to the cylindrical cliff, the center, and other objects. Afterwards, participants completed variable numbers of trials (mean number of trials ± standard error of the mean (SEM), 229 ± 5), depending on individual movement speed. Each trial consisted of a retrieval and a subsequent re-encoding phase (Fig. 1A). During the retrieval phase, participants were shown one of the eight objects ("Cue") and asked to place it as accurately as possible at its initial position ("Response location"; Fig. 1B). Depending on response accuracy, participants then received feedback via one of five possible smiley faces (Fig. S1B). Afterwards, each object had to be collected again from its initial position ("Correct location"; Fig. 1B), allowing for re-encoding. Thus, participants gradually improved their performance throughout the experiment (Fig. S2). After each trial, a fixation crosshair was shown for a variable duration of 3 to 5 sec (uniformly distributed). At the beginning of the first trial (after the initial learning phase), participants started from locations that were similarly central between the two groups (two-sample t-test, t_{73} = -1.107, P = .272). Subsequent starting positions of all retrieval phases were identical with the self-paced end positions of the directly preceding re-encoding phases to ensure a continuous, more natural navigation course. Note that these end positions were not completely identical with the object positions since participants only needed to enter a circle with a radius of 120 virtual units around each object to "collect" it. Every 0.1 sec, the position of the participant in the arena was logged, which allowed us to extract movement periods, movement speed and movement direction. The virtual arena was projected onto a screen positioned at the head of the magnet bore and reflected onto a mirror attached to the head coil.

MRI data acquisition

Scanning was performed at the German Center for Neurodegenerative Diseases (DZNE), Bonn, using a *Skyra* 3-T MRI scanner (Siemens, Erlangen, Germany) with a 20-channel head receive coil. Participants underwent a T1 weighted structural scan and a T2*-weighted functional scan. For T1-weighted structural brain imaging, a whole-head magnetization-prepared rapid gradient-echo imaging sequence (MP-RAGE) with the following parameters was used: 1 mm isotropic resolution; inversion time (TI) = 1100 ms; repetition time (TR) = 2500 ms; echo time (TE) = 4.37 ms; flip angle = 7°; total acquisition time (TA) = 5:08 min. Functional images were subsequently acquired using a T2*-weighted echo-planar-imaging (EPI) protocol, adapted to account for increased susceptibility-induced artifacts in inferior slices (*33*), with the following parameters: acquisition matrix = 64 x 64; TR = 2600 ms; field of view = 192 mm x 192 mm; flip angle = 82°. Forty 2 mm-thick transversal slices were acquired in ascending order (1 mm slice gap) within each TR. The anterior-posterior phase encoding direction was tilted by 30° towards the coronal plane (lifted anterior end). The echo time for superior slices was set to TE_{max} = 31 ms while the echo time for inferior slices was set to TE_{min} = 23 ms with a linear increase from the 14^{th} to the 24^{th} slice. The fMRI time series comprised six sessions, each consisting of 305 images (TA = 13:13 min per session). The first five images of each session were excluded from data analysis to account for signal steady-state transition.

Data analysis

Matlab (2014a, The MathWorks Inc., Massachusetts) was used to perform behavioral analyses. Freesurfer (v5.3.0, http://surfer.nmr.mgh.harvard.edu/) enabled the creation of participant-specific anatomical ROIs and was used to obtain four structural measures of right entorhinal cortex (volume, thickness, mean curvature, and surface area). SPM8 (http://www.fil.ion.ucl.ac.uk/spm) served to perform all first level analyses of functional MR images as well as the confirmatory second level analysis of compensatory activity on whole brain level. SPSS (version 22.0, IBM Corp., NY) was used to calculate all other second-level statistics. Most data were normally distributed and variance was similar between groups. Otherwise, non-parametric test statistics and corrections for unequal variances were chosen. All second-level statistics were two-sided.

Behavioral analyses

First, we assessed participant-specific spatial memory performance by averaging the distances between response and correct locations across trials ("drop error", Fig. 1B). Solely for visualization and enhanced readability, we converted these "drop errors" into values of spatial memory performance using the following formula: spatial memory performance$_i$ = [max(drop error) - drop error$_i$ + min(drop error)] / max(drop error), where max(drop error) and min(drop error) correspond to the maximum and minimum drop error across all participants, respectively, and drop error$_i$ corresponds to the drop error in participant *i*. This formula simply reverses the drop errors and maps them into the range between 0 and 1. Second, participant-specific values of central navigational preference were calculated as central navigational preference = n_{center} / $n_{periphery}$, where n_{center} is the number of time points spent in the center of the arena and $n_{periphery}$ is the number of time points spent in the periphery of the arena. The division between center and periphery was drawn by dividing the arena radius into two equal halves. Only time points during the retrieval phase were considered, as we expected a behavioral relevance for correct object placement solely during this trial phase. Drop error values and central navigational preference values were entered into two-sample *t*-tests between genetic subgroups. The result of the central navigational preference values was corrected for unequal variances (assessed via Levene's test for equality of variances) using the Welch-Scatterthwaite method as implemented in SPSS by default. To validate our metric of central navigational preference, we determined the absolute distances of the self-paced starting positions as well as all self-paced positions relative to the center and compared them between genetic subgroups using two-sample *t*-tests. Third, as control analyses, we calculated basic behavioral characteristics including the number of movement time points, the cut-off speed (used for the definition of fast movements, see analysis of grid-cell-like representations below), the total path length, the total number of trials, the average duration of retrieval-phases, and the average duration of re-encoding-phases. Potential differences between these characteristics as a function of genotype were tested (Table S2). Finally, learning curves were calculated across participants of both genetic subgroups. For visualization and statistical evaluation with a time × genotype repeated measures ANOVA, drop error times were assigned to one-minute-bins and corresponding drop errors averaged within bins, leading to 77 drop error values per participant (Fig. S2).

Pre-processing of functional images

SPM8 within Matlab was used to pre-process each participant's fMRI data. Functional images were spatially realigned, unwarped, slice time corrected and coregistered onto participant-specific anatomical T1 images. For the analysis of grid-cell-like representations (Fig. 2B), stability metrics (Fig. 3), and task-related activity (Fig. 2C, Fig. S8), we did not apply normalization as we exclusively performed ROI analyses and aimed at minimizing post hoc spatial distortions of the data. Only for the "confirmatory analysis of compensatory mechanisms" (see below; Fig. S9), we applied normalization to Montreal Neurological Institute (MNI) space using parameters from the segmentation of the T1 structural image (*34*). Images were spatially smoothed with an isotropic 6 mm full-width-half-maximum Gaussian kernel.

Creation of participant-specific anatomical ROIs

To improve the accuracy of the ROI analyses, normalization was replaced by the usage of participant-specific anatomical ROIs (right, left, and bilateral EC; right, left, and bilateral hippocampus; right, left, and bilateral posterior hippocampus; right, left, and bilateral amygdala; right, left, and bilateral fusiform gyrus; right, left, and bilateral precentral cortex) created via the Freesurfer image analysis suite (see Fig. 2D for exemplary ROIs of right EC, right amygdala and bilateral hippocampus). The right EC ROI was used in the analysis of grid-cell-like representations. The right hippocampal and right amygdala ROIs were used to perform control analyses in control participants as they are adjacent regions of the right EC. Finally, the other ROIs served for the analysis of task-related activity. Briefly, processing included registration to Talairach space, intensity normalization, skull stripping, volumetric labelling, and cortical parcellation. The detailed procedure has been described and validated in previous publications (*35*-*37*) and is comparable in accuracy to manual labelling (*38*). Afterwards, Freesurfer output was transformed back into participant-specific space to establish compatibility with the coregistered, smoothed functional images. Next, the parcellated cortical ribbon was used to obtain ROIs of EC, fusiform gyrus, and precentral cortex, whereas the segmented subcortical structures were used to produce ROIs of hippocampus and amygdala. All participants' ROIs were visually inspected by overlaying them onto the participant-specific anatomical T1 image to ensure proper definition. The number of voxels of our main target ROIs did not differ between genetic subgroups (two-sample *t*-test for right EC, t_{73} = -1.309, P = .195, mean number of voxels ± SEM: 1704 ± 60 in control participants, 1811 ± 55 in risk participants; two-sample *t*-test for bilateral hippocampus, t_{73} = -.789, P = .432, mean number of voxels ± SEM: 9062 ± 155 in control participants, 9225 ± 136 in risk participants) and were in accordance with previous findings (right EC, mean ± SEM, 1759 ± 41, see ref. *39*; bilateral hippocampus, mean ± SEM, 9144 ± 103, see ref. *40*). Furthermore, the voxel numbers of all other ROIs that were additionally used also did not differ between genetic subgroups (two-sample *t*-tests, all $P > .05$).

Analysis of grid-cell-like representations

The analysis of grid-cell-like representations followed the procedure of Doeller et al. (*15*): The data was split into two halves. By fitting a first general linear model (GLM) to the first half of the data (Fig. 2A, left panel), we identified the angular orientation of the putative grid axes relative to the environment in each participant's right EC (Fig. 2A,

middle panel; Table S4), because the angular orientation is not known a priori. Afterwards, we modeled the second half of the data with a second GLM to contrast brain activity during aligned movements with brain activity during misaligned movements relative to the previously identified putative grid axes from the first half of the data (Fig. 2A, right panel; Table S5). This procedure is explained in greater detail hereinafter. The a priori defined first half of the data (sessions 1, 3, and 5) was modeled with a first GLM including a regressor for all fast movement time points (see below) in the virtual arena and regressors of no interest modeling phases without navigation in the environment (Table S4). Two parametric modulators of the movement regressor modeled the movement direction at each movement time point: $\sin[\alpha(t) * 6]$ and $\cos[\alpha(t) * 6]$, where $\alpha(t)$ is the movement direction at time point t (Fig. 2A, left panel), arbitrarily aligned to 0° of the virtual reality environment as defined by the background cues. Multiplying by six transforms the movement directions into 60° space to account for the six-fold rotational symmetry of potential grid-cell-like representations. In other words, the factor 6 means that these regressors are sensitive to activation showing a six-fold rotational symmetry in running direction (i.e., activation with six evenly spaced peaks as a function of running direction will produce parameter estimates β_1 and β_2 for the two regressors with large amplitude $\text{sqrt}(\beta_1^2 + \beta_2^2)$). Next, the β-values of the two parametric modulators were extracted from the right EC ROI to calculate its putative mean grid orientation in 60° space (varying between -180° and 180°): mean grid orientation $\varphi_{60°} = \arctan(\beta_1/\beta_2)$, where β_1 = averaged beta value for $\sin[\alpha(t) * 6]$ and β_2 = averaged beta value for $\cos[\alpha(t) * 6]$ across voxels of the right EC ROI. Dividing by six changed the mean grid orientation $\varphi_{60°}$ back into normal 360° space (varying between -30° and 30°). Adding n times 60° yielded all putative grid axes (Fig. 2A, middle panel). Afterwards, we looked for sinusoidal modulation of activation with six-fold rotational symmetry in the other half of the data. In detail, this means that a second GLM was applied to the a priori defined second half of data (sessions 2, 4, and 6) containing regressors for "aligned" (within ± 15° of the nearest axis of the grid) and "misaligned" (more than ± 15° from a grid axis) movements in the virtual arena (Fig. 2A, right panel; Table S5). Contrast values (aligned > misaligned) were extracted from the right EC ROI and averaged across voxels within participants. More positive values indicate more pronounced grid-cell-like representations, whereas smaller or even negative values indicate less pronounced grid-cell-like representations. Please note that we restricted our analysis to the right EC and fast movements (fast tertile of all movements, separately determined for each participant, lower boundary defined as "cut-off speed", see Table S2), following Doeller et al. (*15*).

Control analyses of grid-cell-like representations

In control participants, we performed two control analyses to validate both the specificity of six-fold rotational symmetry and the specificity of the right EC ROI. To test for the specificity of the six-fold symmetric sinusoidal modulation, we used the same analysis procedure of (1) estimating the mean grid orientation of the right EC and (2) looking for sinusoidal modulation in control models, however with directional periodicities of 120°, 90°, 72°, 51.4°, and 45° (that is, three-fold, four-fold, five-fold, seven-fold, and eight-fold rotational symmetry) respectively. To test for the specificity of the right EC ROI, we performed the analysis with 6-fold rotational symmetry in right

hippocampus and right amygdala, since they are adjacent regions of the right EC (for the results, see Fig. S3).

Session-wise analysis of grid-cell-like representations

To evaluate whether grid-cell-like representations were also reduced under the conditions of similar temporal and spatial stability of the voxel-wise grid orientations between genetic subgroups, we applied the analysis of grid-cell-like representations (see above) on shorter data segments: one session served to identify the angular orientation of the putative grid axes and the subsequent session served to contrast brain activity during movements aligned with these grid axes versus brain activity during misaligned movements, leading to five session combinations (estimate grid orientation in session 1, calculate contrast of aligned versus misaligned movements in session 2; same between session 2 and session 3; session 3 and session 4; session 4 and session 5; session 5 and session 6). Temporal and spatial stability values were assessed for each session combination following the procedure explained below. The results were averaged across session combinations before entering group statistics.

Linear multiple regression to predict spatial memory performance

To investigate whether grid-cell-like representations and central navigational preference were related to spatial memory performance, we calculated a linear multiple regression model with spatial memory performance as the dependent variable. Grid-cell-like representations, central navigational preference, genotype, sex, and age were included as relevant predictor variables. Concerning grid-cell-like representations, we hypothesized a positive influence on spatial memory performance as shown before (*15*).

Analysis of task-related activity

Hippocampal task-related activations were estimated using a separate GLM including a regressor that modeled the time during which participants were engaged in the task (i.e., cue, retrieval, feedback, and re-encoding combined; Table S6). Contrast values for this regressor versus the implicit baseline were extracted from the participant-specific right, left, and bilateral hippocampal ROIs (created using Freesurfer, see above) and averaged across voxels within participants ("hippocampal task-related activation"). Afterwards, we examined whether reduced right EC grid-cell-like representations were related to increased hippocampal task-related activity across all participants by calculating a Pearson correlation. To further elucidate the relationship between grid-cell-like representations and other ROIs inside and outside the medial temporal lobe, task-related activations were also extracted from EC, amygdala, fusiform gyrus, and precentral cortex (created using Freesurfer) and correlated to the grid-cell-like representations (Fig. S8) using Pearson correlations.

Analysis of potentially compensatory mechanisms

To elucidate whether our finding of increased hippocampal task-related activity reflects compensatory mechanisms with a behavioral impact, we conducted two analyses. First, we calculated six different versions of the linear multiple regression (Table S3) used to predict spatial memory performance in the main text (Table 1). Each version included task-related activity of a different part of the hippocampus (bilateral

hippocampus, left hippocampus, right hippocampus, bilateral posterior hippocampus, left posterior hippocampus, right posterior hippocampus) as an additional independent variable. We were specifically interested in the influence of task-related activity of the posterior hippocampus, since this is the region of the hippocampus that has been shown to be especially relevant for spatial navigation (*22*, *41-45*). Second, we performed a separate second-level whole brain analysis using SPM. Here, first level contrast-images represented trial-by-trial response accuracy within participants (see below: "Confirmatory analysis of compensatory mechanisms"). See below for the results.

Confirmatory analysis of compensatory mechanisms

To validate our result of compensatory hippocampal activity, we used an additional whole-brain approach that identified voxels which were specifically relevant for correct object placement (i.e., good spatial memory performance) and that were also negatively correlated to grid-cell-like representations. This approach contained a first level GLM and a second level analysis in SPM. Hence, exclusively for this analysis, pre-processing of functional images included normalization to MNI space before smoothing. On the first level, the GLM contained one regressor of the retrieval-phase that was modeled with a parametric modulator depicting the accuracies of the trial-specific response locations (Table S7) revealing voxels associated with good spatial memory performance. Contrast images of the parametric modulator versus zero were calculated for all participants and entered into a second level linear regression model in SPM. This linear regression model contained the participant-specific grid-cell-like representations of right EC as predictor variable. We then identified voxels which were negatively correlated with grid-cell-like representations across the group of participants, also reflecting potential compensatory mechanisms. Based on our strong a priori hypothesis, we applied small volume correction (SVC) for bilateral hippocampus (SPM anatomy toolbox mask image; mask volume = 23,664 mm^3). We report activation at $P < .05$ at the peak level corrected for multiple comparisons within this search volume.

Calculation of temporal and spatial stability

Grid-cell-like representations solely occur when the voxel-wise grid orientations (angular orientation of the putative grid axes relative to the environment in 60° space) from the first half of the data exhibit both spatial and temporal stability. Thus, in principle, reduced grid-cell-like representations can be either due to spatial or temporal instability of the voxel-wise grid orientations (or – similar temporal and spatial stability between genetic subgroups in smaller data segments provided – due to a relatively weaker right EC contrast of aligned versus misaligned movements, which we investigated using shorter data segments, see main text and above: "Session-wise analysis of grid-cell-like representations"). For each participant, we calculated one spatial stability value (statistically expressed as Rayleigh's *z*-value: the higher the *z*-value, the higher spatial stability) and one temporal stability value (estimated as percentage values: the higher the percentage value, the higher temporal stability). This is explained in greater detail henceforth. Spatial instability is maximal for a uniform circular distribution of grid orientations across voxels. As a result of spatial instability, the mean grid orientation of the first half of the data would be a random selection of this distribution. Arbitrary allocations of aligned and misaligned movements in the second GLM would be the

consequence, leading to reduced or absent grid-cell-like representations. Statistically, spatial stability was evaluated with Rayleigh's test for non-uniformity of circular data (*46*), which was applied to the voxel-wise grid orientations of the first half of the data (accounting for spatial smoothing). This resulted in participant-wise *z*-values of spatial stability (for two examples, see Fig. 3C). In contrast, temporal instability means that the voxel-wise grid orientations – albeit potentially spatially stable – change across time. Incorrect allocations of aligned and misaligned movements in the second GLM would be the consequence, also producing reduced or absent grid-cell-like representations. To obtain a metric of temporal stability, we first calculated the voxel-wise grid orientations in the right EC ROI separately for both halves of the data. Afterwards, we evaluated for each voxel individually whether the grid orientation of the second half of the data was within a range of ± 15° around the grid orientation of the first half of the data. This allowed us to calculate the percentage of voxels with temporally stable grid orientations for each participant (for two examples, see Fig. 3A). For statistical comparison, percentage values ($percentage_{original}$) were logit-transformed according to: $percentage_{new} = \log[percentage_{original} / (1 - percentage_{original})]$, because they were in a limited range of 0 to 1 originally. For group statistics, temporal stability values (i.e. logit-transformed percentage values) and spatial stability values (i.e. Rayleigh's *z*-values) were entered into separate two-sample *t*-tests between genetic subgroups and into separate Pearson correlation analyses to detect significant relations to the grid-cell-like representations. Note that the terms "grid axes" and "grid orientation" used throughout the main paper and the Supplementary Information are based on a directionally modulated fMRI signal and do not simply correspond to electrophysiological nomenclature.

Functional connectivity between EC and hippocampus

Functional connectivity was analyzed by first extracting the preprocessed BOLD time series from right EC and right hippocampus and averaging them across voxels within each of the ROIs (right EC and right hippocampus). Next, linear trends of the time series were removed within sessions and the time series were normalized within sessions to have mean 0 and standard deviation 1. We calculated the Pearson correlation *r* value between the time series of right EC and right hippocampus for each participant and transformed the *r* values into *z* values (Fisher-*z*-transformation). As a control analysis, we included the participant-specific head motion parameters as regressors of no interest. As a second control analysis, functional connectivity between right EC and bilateral hippocampus as well as between right EC and left hippocampus was also calculated using the identical procedure.

Supplementary Text

Grid-cell-like representations and spatial memory performance within genetic subgroups

In the main text we showed that multiple regression was sensitive to reveal a positive relationship between the magnitude of grid-cell-like representations and spatial memory performance across all participants. To further evaluate a potential dependency of this relationship on genotype that would be relevant to proposing a mechanistic account of (later) spatial memory impairments observed in AD, we conducted two exploratory analyses. First, we plotted the raw bivariate correlations between grid-cell-like representations and spatial memory performance, separately for both genetic subgroups (Fig. S6A). Visual inspection suggests a stronger relationship in risk participants, but this was not significant (risk participants only: Pearson's r = .204, P = .220; control participants only: Pearson's r = .055, P = .748; difference between correlation coefficients, z = .63, P = .529). Second, we used partial correlations as a more sensitive approach correcting for sex, age, and central navigational preference, which revealed a significant partial correlation in risk participants (r = .341, P = .045; Fig. S6B), but not in control participants (r = .086, P = .628), with no difference between both groups (z = 1.12, P = .263). Thus, the most robust finding is an overall positive effect of grid-cell-like representations on spatial memory performance that is influenced by other factors such as sex, age, and central navigational preference as represented in the linear multiple regression analysis (Table 1).

Hippocampal task-related activity and spatial memory performance

To elucidate whether our finding of increased hippocampal task-related activity reflects compensatory mechanisms with a positive impact on behavior or adverse effects with a negative behavioral impact, we conducted two additional analyses (see Methods). First, different versions of the linear multiple regression (Table 1, including task-related activity of different parts of the hippocampus as an additional predictor, see Methods) showed that task-related activity of the entire hippocampus is too unspecific to reveal a positive association with spatial memory performance (bilateral, P = .660; left, P = .465; right, P = .855; Table S3, Models 1-3). However, activity in the posterior hippocampus (posterior third of the hippocampus), which seems to be more closely related to spatial navigation than the anterior hippocampus (*22*, *41-45*), was associated with improved spatial memory performance, in particular in the left hemisphere (bilateral, P = .068; left, P = .006; right, P = .517; Table S3, Models 4-6). This specificity was supported by our second-level whole brain analysis of voxels which are positively associated with spatial memory performance (within participants) and that are at the same time negatively associated with grid-cell-like representations (across participants; see Methods: "Confirmatory analysis of compensatory mechanisms"). This analysis revealed a brain-wide peak in the left posterior hippocampus (peak MNI coordinates: -18/-28/-8, peak z-score = 4.03, P = .038, FWE-corrected after small volume correction for the bilateral hippocampus; Fig. S9). Importantly, no other voxel exceeded this z-value on the whole brain level, reflecting the specificity of activation in the posterior hippocampus. Taken together, these two analyses suggest compensatory hippocampal task-related activity that is specific to its posterior third.

Interpretation of increased activity in *APOE*-ε4-carriers

It is a matter of ongoing debate whether increased hippocampal activity in *APOE*-ε4-carriers represents compensatory mechanisms required to maintain normal cognitive functioning or, in contrast, pathological dysfunction. Compensatory mechanisms in ε4-carriers were first suggested by Bookheimer et al. (*19*), similar to the finding of potential compensatory mechanisms in patients with mild AD (*47*) that could indeed be related to better performance (*48*). The hypothesis of compensatory mechanisms was further supported by findings of Bondi et al. (*49*), Rosano et al. (*50*), Han et al. (*51*), Filippini et al. (*21*), Wierenga et al. (*52*), and Suthana et al. (*53*). Even in a 20-year-old at risk for familial AD (presenilin 1 mutation carrier) increased brain activity within memory-related neural networks (including the hippocampus) was found and interpreted as compensatory effort (*54*). However, increased brain activity was also discussed as indicating different cognitive processing strategies, biochemical alterations, or as a marker of the pathophysiologic process itself (*55-57*). Moreover, there is growing evidence that hippocampal hyperactivity in mild cognitive impairment, AD, and presymptomatic individuals is a paradoxical or even adverse condition that could be targeted therapeutically (e.g., *58, 59*). Jagust et al. (*60*) propose that lifespan brain activity in humans increases deposition of amyloid-β. Bakker et al. (*23*) even show that the reduction of hippocampal hyperactivity by the antiepileptic drug levetiracetam improves cognition in amnestic mild cognitive impairment. Furthermore, it is shown in mouse models that neuronal activity increases the regional load of amyloid-β deposition (*24*).

In the main text, we proposed that our finding of increased hippocampal activity indicates compensatory mechanisms in risk participants. This interpretation was based on our findings that reduced grid-cell-like representations were correlated with increased hippocampal task-related activity, and that this relationship was significantly more pronounced in risk participants as compared to control participants in the posterior hippocampus. In principle, there must be some compensatory processes given our contrary findings that spatial memory performance is preserved in risk participants, although they show reduced grid-cell-like representations and reduced central navigational preference, which are both related to impaired spatial memory performance across all participants. Increased hippocampal activity could reflect a more pronounced boundary-based navigation strategy in risk participants (*61, 28*) or enhanced hippocampal path integration computations (*29, 30*) to compensate for impaired entorhinal path integration. Furthermore, our finding that reduced grid-cell-like representations are also related to increased task-related activity in EC and amygdala (Fig. S8) could be interpreted as an overall compensatory activity of the medial temporal lobe areas. For example, Filippini et al. (*21*) speculate that increased activity in hippocampal regions reflects compensation of reduced synaptic plasticity, neuronal growth, or altered long-term potentiation, which seems to be particularly affected by apolipoprotein E4 (*62*). However, this finding could also speak in favor of an adverse broader disruption of medial lobe network computations accounting in total for our finding of altered navigational behavior in risk participants. Hence, to further elucidate whether our finding of increased hippocampal task-related activity could represent compensatory mechanisms with a behavioral impact, we conducted two additional analyses (see Supplementary Text

"Hippocampal task-related activity and spatial memory performance"). It became apparent that increased task-related activity specifically of the (left) posterior hippocampus is related to better behavioral performance, supporting the compensatory hypothesis. Furthermore, our finding of reduced functional connectivity between EC and hippocampus in participants with reduced temporal stability values (Fig. S10B) might reflect a mechanism to protect hippocampal processing from impaired entorhinal computations enabling independent compensatory mechanisms. However, the last two results were obtained across all participants and were not modulated by genotype (no differences between correlation coefficients were observed). While this speaks against a compensatory role that is specific to risk participants, it is consistent with the general idea that entorhinal cortex dysfunction is associated with (and possibly responsible for) broader changes in medial temporal lobe computations. In this light, *APOE*-ε4 may induce entorhinal dysfunction that could then, in turn, gradually lead to functional changes in downstream areas. Finally, we would like to point out that the two interpretations of increased hippocampal activity as a compensatory or a pathological phenomenon are not mutually exclusive: increased hippocampal activity could (temporarily) serve as a compensatory mechanism – in particular in young participants, decades before potential disease onset – and simultaneously promote pathological processes. The compensatory potential might then fade out with proceeding pathology or might be shifted to neocortical areas as suggested in various studies (e.g., *53*).

Functional connectivity between right EC and hippocampus

We found that there was pronounced functional connectivity between right EC and right hippocampus across all participants (one-sample *t*-test, $t_{74} = 36.561$, $P < .001$). Furthermore, reduced temporal stability values were associated with lower connectivity values (Pearson's $r = .298$, $P = .009$; Fig. S10B), possibly indicating a decoupling of both regions associated with entorhinal dysfunction. This decoupling between right EC and right hippocampus could constitute a modulating mechanism to reduce the influence of impaired entorhinal computations on hippocampal processing. Independent hippocampal functioning may thus be enabled that could compensate for EC failure. For completeness, similar results were achieved when using the time series from right EC and bilateral hippocampus (correlation to temporal stability values: Pearson's $r = .272$, $P = .018$) or right EC and left hippocampus (correlation to temporal stability values: Pearson's $r = .229$, $P = .048$). Likewise, including the participant-specific head motion parameters (as potential confounds of functional connectivity) did not change the results substantially (correlation between temporal stability values and functional connectivity between right EC and right hippocampus, Pearson's $r = .282$, $P = .014$).

Potential mechanistic basis of reduced grid-cell-like representations in risk participants

We speculate that risk participants exhibit less robust grid-cell-like representations and temporally unstable grid orientations in combination with preserved spatial stability of the grid orientations because of the underlying neuropathological changes: Intraneuronal neurofibrillary tangles – potentially impairing grid cell inherent properties such as temporal stability and strength of the grid representations – and not interneuronal amyloid-β plaques – possibly affecting synaptic communication between grid cells and thus spatial stability of the grid orientations – appear first in

histopathological sections, especially in *APOE*-ε4-carriers (*6*, *7*). These hypotheses could be tested in mouse models of AD.

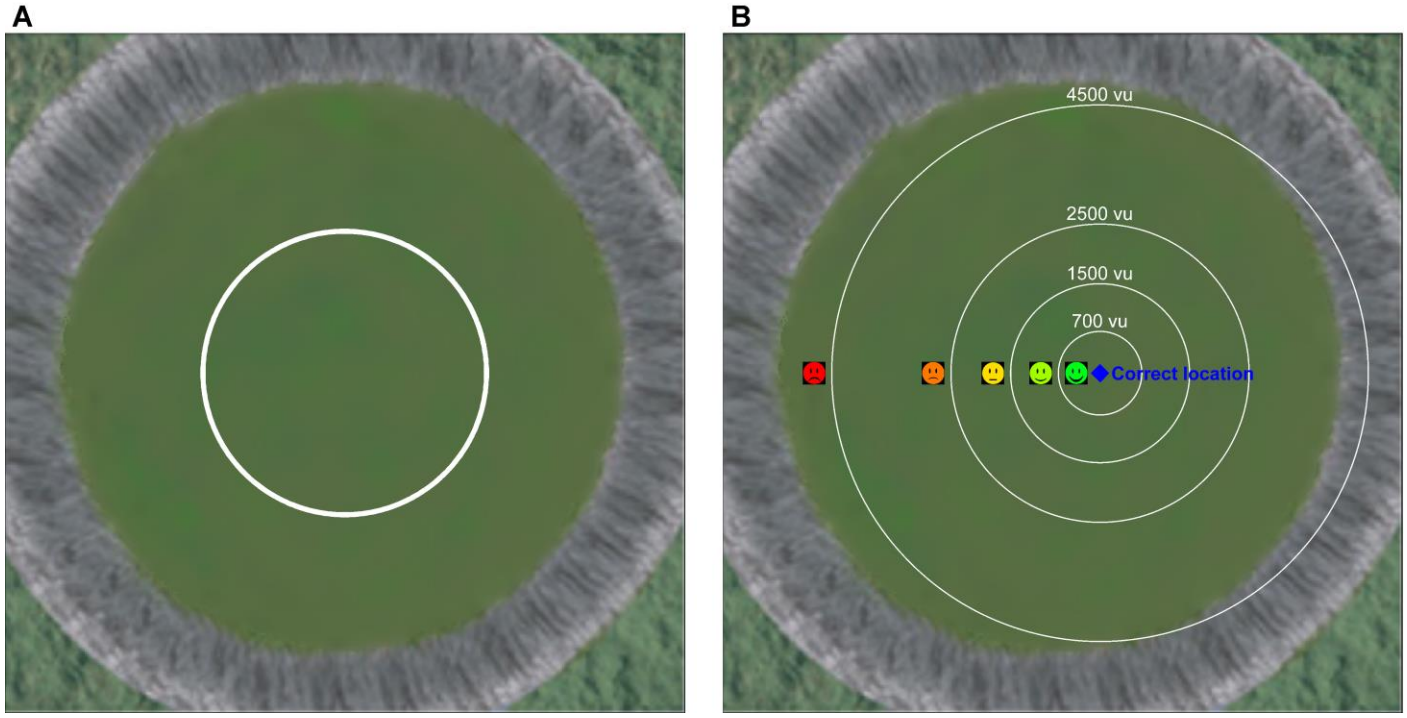

Fig. S1. Illustration of central navigational preference and feedback. (**A**) Participant-specific values of central navigational preference were calculated as central navigational preference = n_{center} / $n_{periphery}$, where n_{center} is the number of time points spent in the center of the arena (within circle) and $n_{periphery}$ is the number of time points spent in the periphery of the arena (outside circle). The division into center and periphery was drawn by dividing the arena radius into two equal halves. Solely time points during the retrieval phase were considered, as we expected a behavioral relevance for correct object placement only during this trial phase. (**B**) After placement of the object, participants received feedback via one of five smiley faces. E.g., dark green smiley faces were shown when the participant placed the object within a radius of 700 virtual units (vu) around the correct object location.

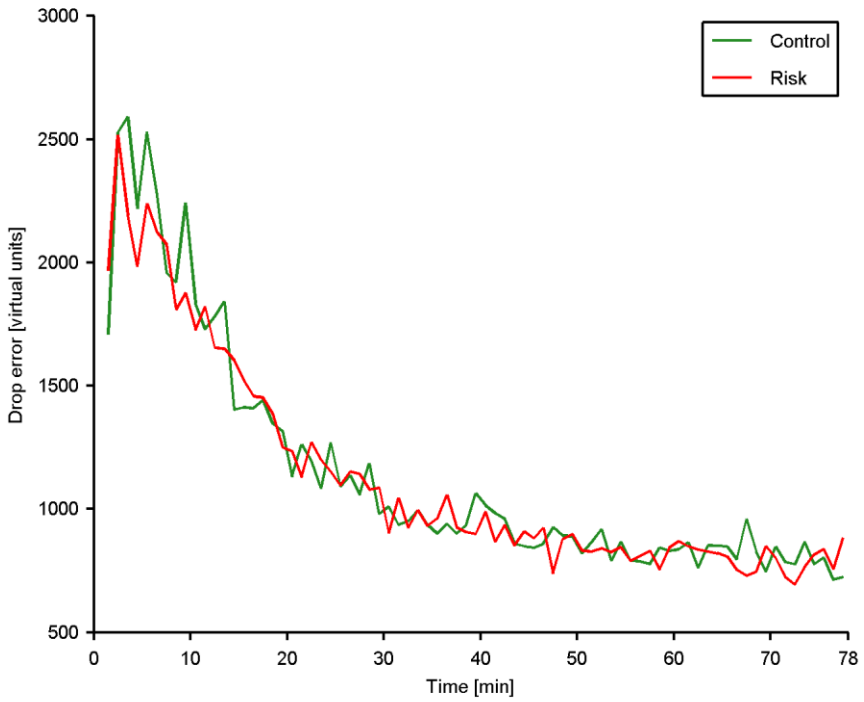

Fig. S2. Learning curves. Participants gradually improved their performance throughout the experiment. As expected, drop errors decreased with time. However, they did not vary as a function of genotype or time-genotype-interaction (time × genotype repeated measures ANOVA: main effect of time, $F_{76,5548} = 32.326$, $P < .001$; no main effect of genotype, $F_{1,73} = .031$, $P = .860$; no interaction, $F_{76,5548} = .643$, $P = .993$).

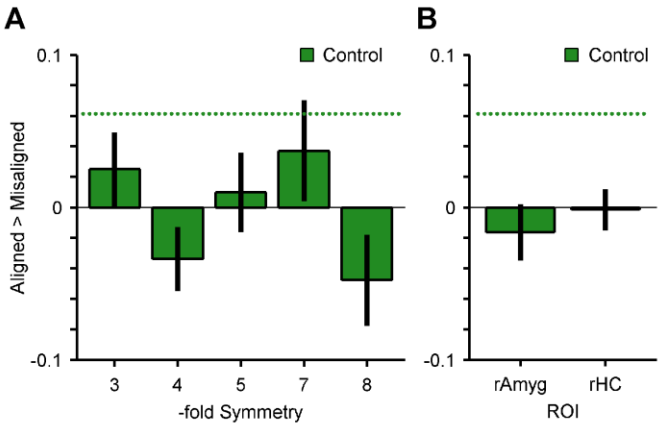

Fig. S3. Control analyses. (**A**) Absence of "Aligned > Misaligned" effects in 3-, 4-, 5-, 7-, and 8-fold rotational symmetry control models for control participants (all $P > .112$). (**B**) 6-fold rotational symmetry in right amygdala ("rAmyg") or right hippocampus ("rHC") does not lead to consistent grid-cell-like representations ("Aligned > Misaligned") in control participants (both $P > .382$). These results show that our finding in control participants is specific for six-fold rotational symmetry and specific for right EC. Green dotted line represents the result of 6-fold rotational symmetry in the right EC of control participants from Fig. 2B. All bars show mean and SEM across participants. Units of all contrasts are parameter estimates.

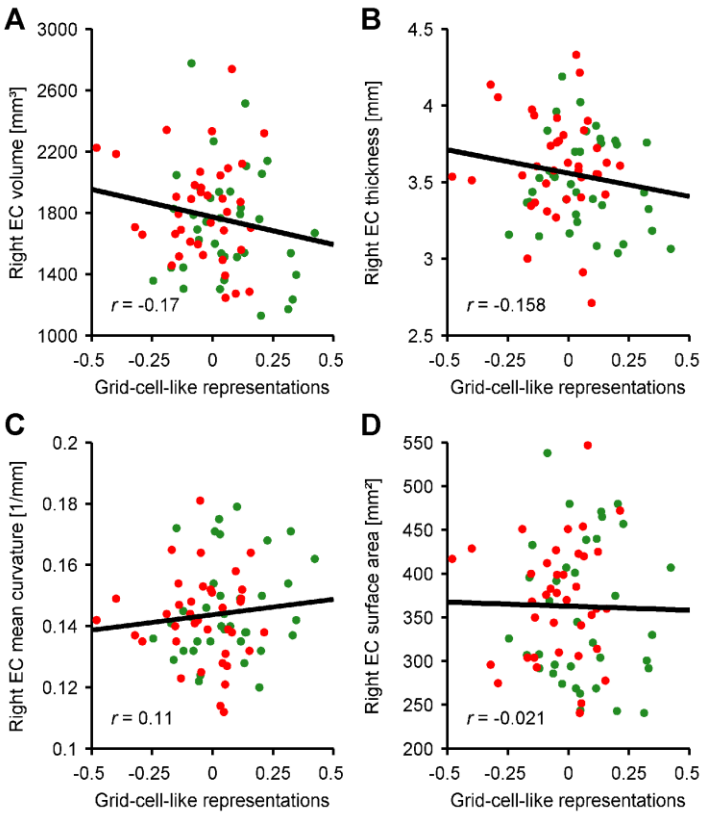

Fig. S4. Grid-cell-like representations and participant-wise structural metrics of the right entorhinal cortex. Pearson correlations did not reveal associations between grid-cell-like representations and right EC structural metrics across participants, which could potentially account for the functional changes: (**A**) volume, $P = .145$, (**B**) thickness, $P = .177$, (**C**) mean curvature, $P = .348$, (**D**) surface area, $P = .861$. Correlation coefficients did not differ between genetic subgroups. Structural metrics were obtained using the Freesurfer image analysis suite (see Methods). Green dots represent control participants, red dots represent risk participants. Units of grid-cell-like representations are parameter estimates.

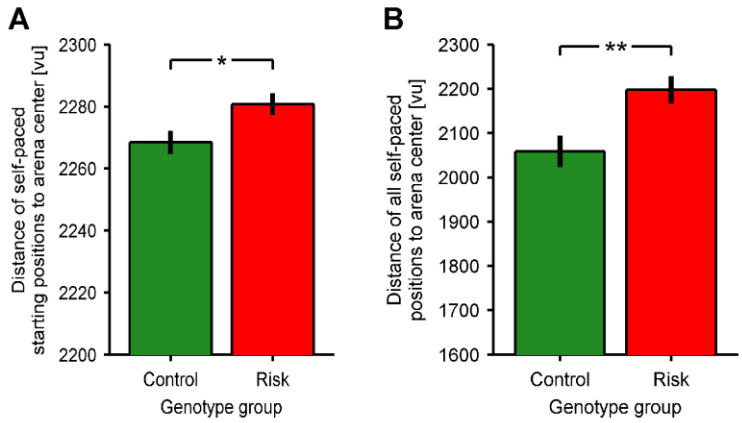

Fig. S5. Absolute distances of the self-paced positions relative to the arena center in the virtual environment. In accordance with our finding of reduced central navigational preference, risk participants exhibited greater mean distances of the (**A**) self-paced starting positions (at the beginning of each retrieval phase, except for the very first retrieval phase) as well as greater mean distances of (**B**) all self-paced positions (during all cue, retrieval, feedback, and re-encoding phases) relative to the arena center of the virtual environment. All bars show mean and SEM across participants. *$P < .05$, **$P < .01$.

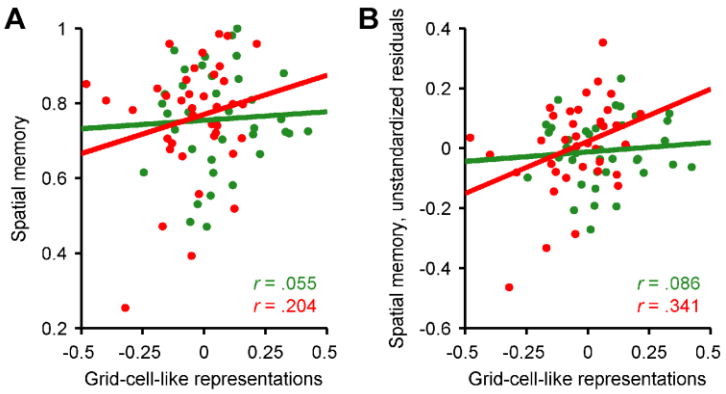

Fig. S6. Grid-cell-like representations and spatial memory performance within genetic subgroups. (**A**) Raw bivariate Pearson correlations between grid-cell-like representations and spatial memory performance. Risk participants only: $P = .220$; control participants only: $P = .748$; difference between correlation coefficients: $z = .63$, $P = .529$. (**B**) Partial correlations between grid-cell-like representations and spatial memory performance correcting for sex, age, and central navigational preference, separately for both genetic subgroups. Risk participants only: $P = .045$; control participants only: $P = .628$; difference between correlation coefficients: $z = 1.12$, $P = .263$. Green dots represent control participants, red dots represent risk participants. Units of grid-cell-like representations are parameter estimates.

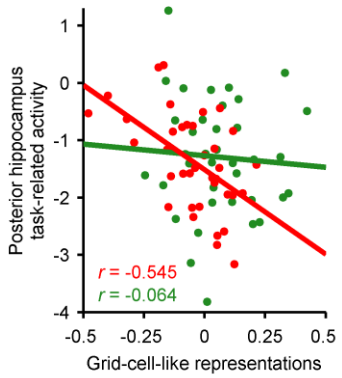

Fig. S7. Genotype dependent relation between task-related activity in the posterior hippocampus and magnitude of grid-cell-like representations. In the posterior hippocampus, the negative correlation between task-related hippocampal activity and the magnitude of grid-cell-like representations is significantly different between genetic subgroups ($P = .023$): Whereas risk participants show a highly significant correlation ($P < .001$), this effect is not present in control participants ($P = .707$). Green dots represent control participants, red dots represent risk participants. Units of grid-cell-like representations and task-related activity are parameter estimates.

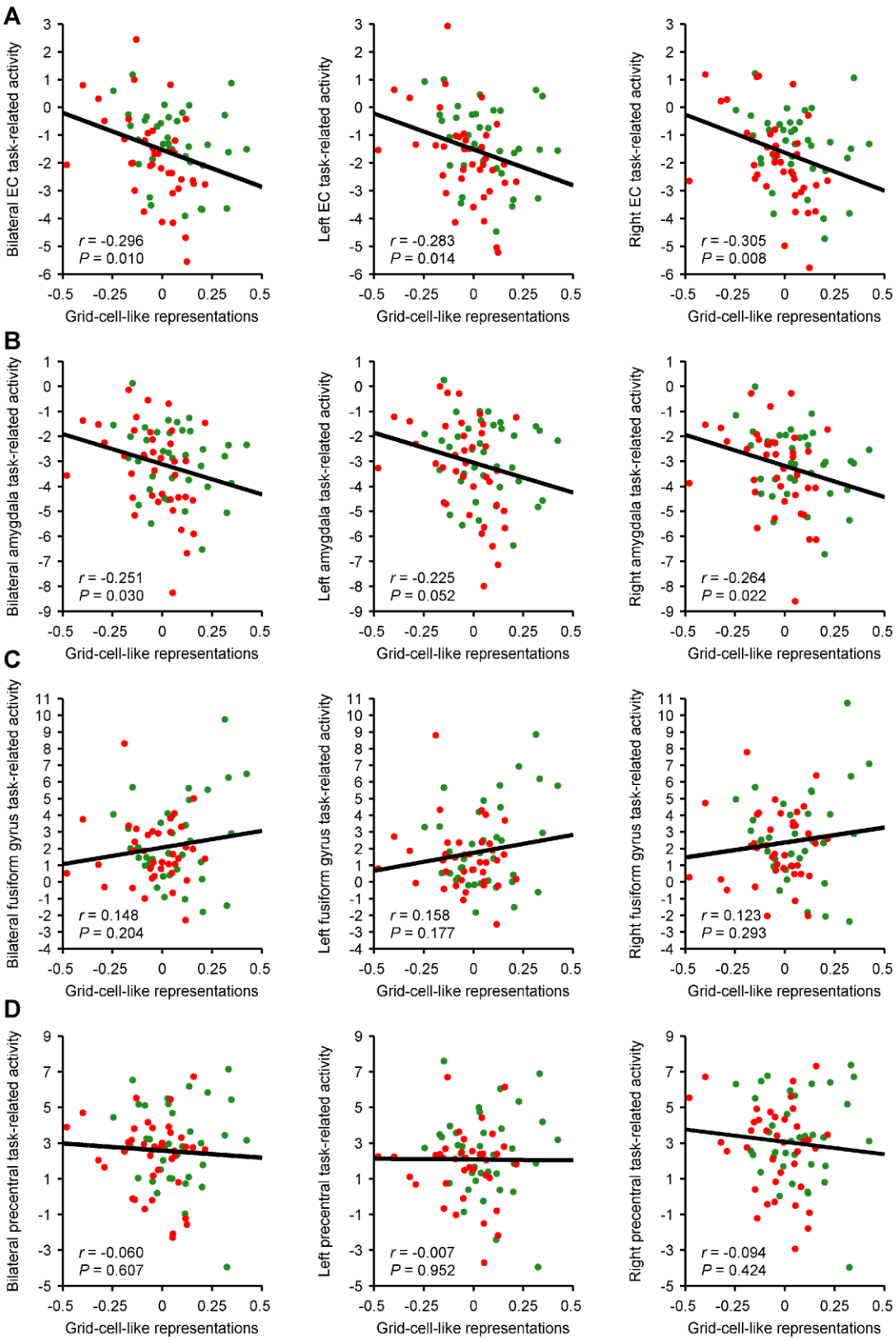

Fig. S8. Grid-cell-like representations and task-related activity. Reduced grid-cell-

like representations were not only related to increased task-related activity in the hippocampus (Fig. 2C), but also to increased task-related activity in EC (**A**) and amygdala (**B**). Fusiform gyrus (**C**) and the precentral cortex (**D**) were chosen as control regions outside the medial temporal lobe. *P*- and *r*-values refer to Pearson correlations. Correlation coefficients did not differ between genetic subgroups. In sum, these data suggest that reduced grid-cell-like representations are related to an overall increase in medial temporal lobe activity. Green dots represent control participants, red dots represent risk participants. Plots on the left show bilateral regions, plots in the middle refer to regions in the left hemisphere, and plots on the right display effects in the right hemisphere. Units of grid-cell-like representations and task-related activity are parameter estimates.

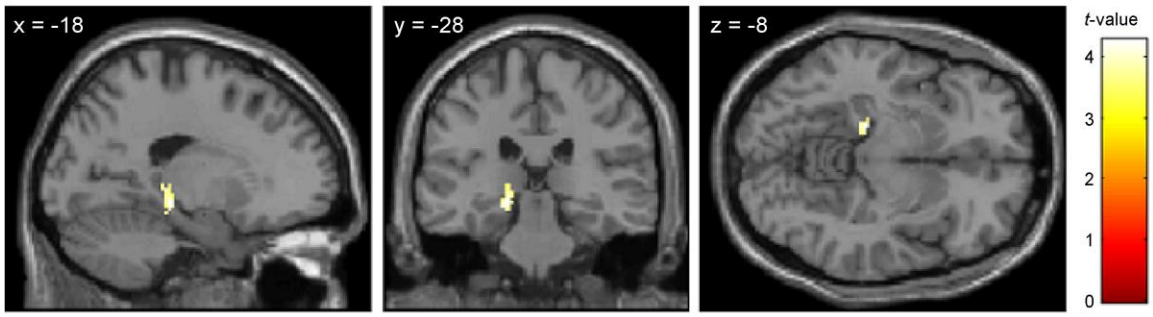

Fig. S9. Confirmatory analysis of compensatory hippocampal activity. Grid-cell-like representations correlated negatively with activity in left posterior hippocampus that was enhanced during trials with more accurate object placement (peak MNI coordinates: -18/-28/-8, peak *z*-score = 4.03, *P* = .038, FWE-corrected after small volume correction for bilateral hippocampus, *t*-image thresholded at *P* < .0005, and voxel extent = 10 for display purposes). No other voxel exceeded this *z*-value on whole brain level. Color bar indicates *t*-statistics. This result supports our previous ROI-result of compensatory hippocampal task-related activity.

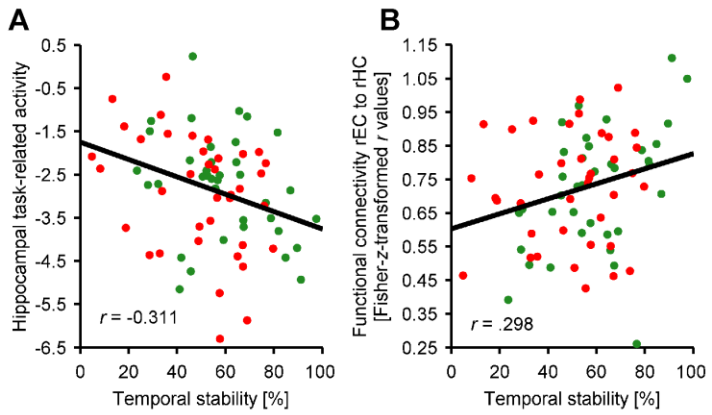

Fig. S10. Temporal stability of voxel-wise grid orientations. (**A**) Higher temporal stability values are significantly correlated with lower hippocampal task-related activity (Pearson correlation, P = .007). (**B**) Reduced temporal stability values are related to decreased functional connectivity between right EC and right hippocampus (Pearson correlation, P = .009). rEC, right entorhinal cortex; rHC, right hippocampus. Green dots represent control participants, red dots represent risk participants.

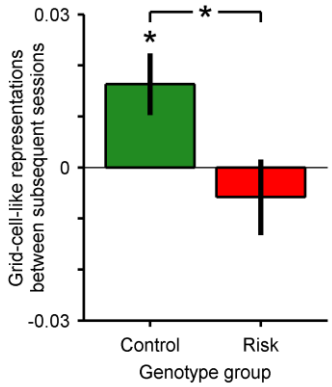

Fig. S11. Grid-cell-like representations under the condition of similar stability values between genetic subgroups. Performing the analysis of grid-cell-like representations on shorter data segments (within subsequent pairs of sessions, see Methods) reveals significant right EC grid-cell-like representations in control participants (one-sample *t*-test, $t_{36} = 2.708$, $P = .010$) but not in risk participants (one-sample *t*-test, $t_{37} = -.788$, $P = .436$), with a significant difference between both groups (two-sample *t*-test, $t_{73} = 2.315$, $P = .023$). In contrast, temporal and spatial stability values do not differ between groups. Bars show mean and SEM across participants. Units of grid-cell-like representations are parameter estimates. *$P < .05$.

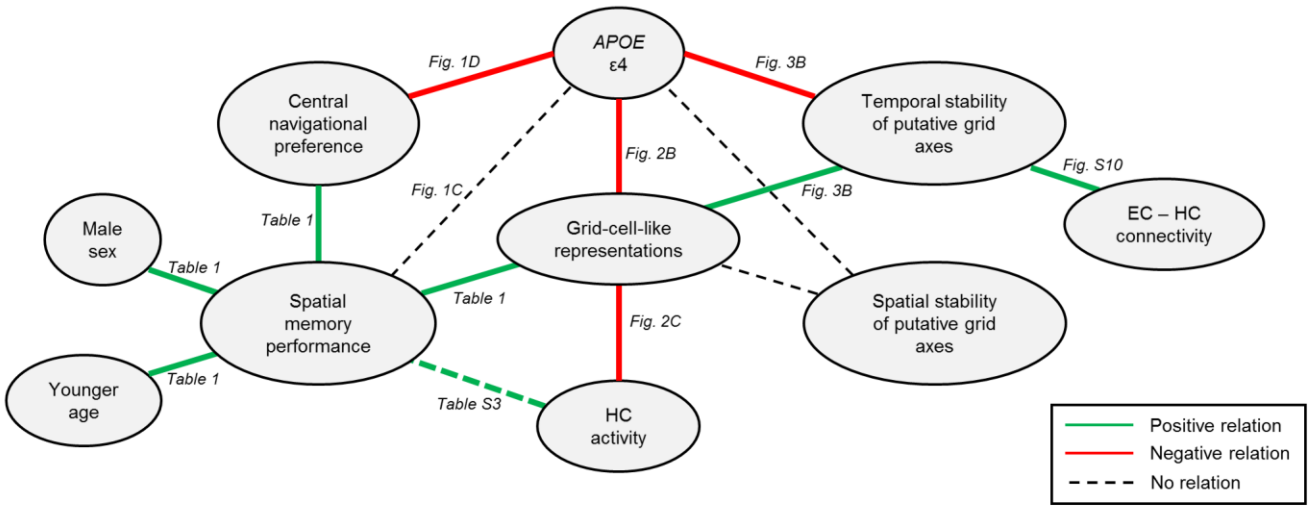

Fig. S12. Schematic overview of all results. EC, right entorhinal cortex; HC, hippocampus. Dashed green line indicates a positive relation between spatial memory performance and HC activity that is specific to the left posterior third of the hippocampus (see Table S3).

Table S1. Demographic characteristics of participants.

	Control group (*APOE* ε3, ε3)	**Risk group (*APOE* ε4, ε3)**	***P***
Number	37	38	
Mean age, age range [years]	22.76 (± .49), 18-30	22.34 (± .45), 18-29	.532[a]
Sex [male/ female]	18/ 19	18/ 20	.912[c]
Education [years]	16.19 (± .38)	16.05 (± .37)	.693[b]
Family history of dementia	2	3	.667[c]

Values denote mean (± SEM) or the number of participants. *P*-values refer to [(a)] two-sample *t*-tests, [(b)] Mann-Whitney *U* tests, or [(c)] χ^2-tests.

Table S2. Influence of *APOE* genotype on basic behavioral characteristics.

	Control group (*APOE* ε3, ε3)	**Risk group (*APOE* ε4, ε3)**	***P***
Number of movement time points [10/s]	19,937 (± 422)	19,967 (± 441)	.961[a]
Cut-off speed [vu/s]	799 (± 1)	799 (± 1)	.611[b]
Total path length [vu]	1,451,250 (± 45,626)	1,447,604 (± 48,265)	.956[a]
Number of trials	229 (± 8.8)	230 (± 6.7)	.918[a]
Duration of retrieval-phases [s]	11.8 (± .7)	11.1 (± .5)	.453[a]
Duration of re-encoding-phases [s]	5.4 (± .3)	5.1 (± .2)	.679[b]

Values denote mean (± SEM). *P*-values refer to [(a)] two-sample *t*-tests or [(b)] Mann-Whitney *U* tests. s, seconds; vu, virtual units.

Table S3. Multiple regression to predict spatial memory performance including task-related activity of different parts of the hippocampus (*N* = 75).

Predictor	β	*t*	*P*
Model 1: including task-related activity in bilateral hippocampus (adjusted R^2 = .161; all VIF < 1.441)			
Grid-cell-like representations	.256	2.093	.040*
Central navigational preference	.235	2.106	.039*
Genotype [control/ risk]	.146	1.230	.223
Sex [male/ female]	-.258	-2.149	.035*
Age [years]	-.304	-2.795	.007**
Task-related activity (bilateral hippocampus)	.057	.442	.660
Model 2: including task-related activity in left hippocampus (adjusted R^2 = .165; all VIF < 1.471)			
Grid-cell-like representations	.270	2.196	.032*
Central navigational preference	.232	2.080	.041*
Genotype [control/ risk]	.154	1.292	.201
Sex [male/ female]	-.242	-2.017	.048*
Age [years]	-.306	-2.826	.006**
Task-related activity (left hippocampus)	.095	.735	.465
Model 3: including task-related activity in right hippocampus (adjusted R^2 = .159; all VIF < 1.347)			
Grid-cell-like representations	.230	1.904	.061(*)
Central navigational preference	.236	2.115	.038*
Genotype [control/ risk]	.134	1.120	.267
Sex [male/ female]	-.290	-2.479	.016*
Age [years]	-.307	-2.816	.006**
Task-related activity (right hippocampus)	-.023	-.183	.855
Model 4: including task-related activity in bilateral posterior hippocampus (adjusted R^2 = .199; all VIF < 1.359)			
Grid-cell-like representations	.278	2.433	.018*
Central navigational preference	.234	2.146	.035*
Genotype [control/ risk]	.167	1.440	.155

Sex [male/ female]	-.178	-1.504	.137
Age [years]	-.311	-2.923	.005**
Task-related activity (bilateral posterior hippocampus)	.225	1.856	.068$^{(*)}$
Model 5: including task-related activity in left posterior hippocampus (adjusted R^2 = .248; all VIF < 1.356)			
Grid-cell-like representations	.286	2.597	.012*
Central navigational preference	.238	2.260	.027*
Genotype [control/ risk]	.173	1.546	.127
Sex [male/ female]	-.123	-1.058	.294
Age [years]	-.308	-2.993	.004**
Task-related activity (left posterior hippocampus)	.334	2.848	.006**
Model 6: including task-related activity in right posterior hippocampus (adjusted R^2 = .163; all VIF < 1.265)			
Grid-cell-like representations	.254	2.160	.034*
Central navigational preference	.235	2.109	.039*
Genotype [control/ risk]	.148	1.253	.214
Sex [male/ female]	-.252	-2.163	.034*
Age [years]	-.307	-2.826	.006**
Task-related activity (right posterior hippocampus)	.078	.651	.517

Multicollinearity was not a concern (see variance inflation factors, VIF). $^{(*)}P < .10$, $*P < .05$, $**P < .010$.

Table S4. Detailed description of the first general linear model (GLM) to identify the angular orientation of the putative grid axes relative to the environment in each participant's right EC. For this general linear model (GLM) one half of the data was used (sessions 1, 3, and 5). All regressors were convolved with the canonical hemodynamic response function (HRF) in SPM before entering the GLM. Data were high-pass filtered at 1/128 Hz. Coefficients for each regressor were estimated for each participant using maximum likelihood estimates.

Regressor	Parametric modulator	Temporal derivative modeled	Duration [seconds]
Regressors to analyze grid-cell-like representations			
Movement		Yes	0
	$\sin[\alpha(t) * 6]$[a]	Yes	0
	$\cos[\alpha(t) * 6]$[a]	Yes	0
Regressors to model trial phases			
Cue	-	Yes	0
Retrieval	-	Yes	Variable
Feedback	-	Yes	0
Re-encoding	-	Yes	Variable
Nuisance regressors			
Scanner drift	-	No	Session[b]
Mean activation	-	No	Session
Head motion parameters	-	No	Session

[(a)] $\alpha(t)$ is angular movement direction at time point t. [(b)] The duration of one session is 13 min.

Table S5. Second GLM to contrast brain activity during aligned movements with brain activity during misaligned movements relative to the previously identified grid axes. For this GLM the other half of the data was used (sessions 2, 4, and 6). All regressors were convolved with the canonical HRF in SPM before entering the GLM. Data were high-pass filtered at 1/128 Hz. Coefficients for each regressor were estimated for each participant using maximum likelihood estimates. The estimated contrast values of aligned versus misaligned movements are termed "grid-cell-like representations".

Regressor	Temporal derivative modeled	Duration [seconds]
Regressors to analyze grid-cell-like representations		
Aligned movement	Yes	0
Misaligned movement	Yes	0
Regressors to model trial phases		
Cue	Yes	0
Retrieval	Yes	Variable
Feedback	Yes	0
Re-encoding	Yes	Variable
Nuisance regressors		
Scanner drift	No	Session
Mean activation	No	Session
Head motion parameters	No	Session

Table S6. GLM to estimate hippocampal task-related activity. All regressors were convolved with the canonical hemodynamic response function (HRF) in SPM before entering the GLM. Data were high-pass filtered at 1/128 Hz. Coefficients for each regressor were estimated for each participant using maximum likelihood estimates.

Regressor	**Temporal derivative modeled**	**Duration [seconds]**
Regressor to model hippocampal task-related activation		
Cue + retrieval + feedback + re-encoding	Yes	Variable
Nuisance regressors		
Scanner drift	No	Session
Mean activation	No	Session
Head motion parameters	No	Session

Table S7. GLM for the confirmatory analysis of compensatory hippocampal activity. The aim of this GLM was to reveal voxel activity associated with spatial memory performance. Hence, we modeled the retrieval phase with a parametric modulator, termed "Response accuracy", which was determined as follows. For each participant separately, the 20%-, 40%-, 60%-, 80%-, and 100%-quantile of all drop errors were calculated. Note that the drop error was defined as the distance between the response location and the correct location (thus having a reverse relation to spatial memory performance). Next, we assigned the highest value of +2 to the parametric modulator, when the trial-specific drop error was in the lowest quantile of all drop errors, the value of +1, when the trial-specific drop error was in the second lowest quantile of all drop errors, and the values 0, -1, and -2, when the trial-specific drop errors were in the middle, second highest, and highest quantile, respectively. All regressors were convolved with the canonical HRF in SPM before entering the GLM. Data were high-pass filtered at 1/128 Hz. Coefficients for each regressor were estimated for each participant using maximum likelihood estimates. Contrast values for the parametric modulator versus zero across all sessions were calculated for all participants and entered into a second level random effects linear regression analysis as implemented in SPM. During the second level analysis, we were then able to look for spatial memory-related brain activations negatively correlated to grid-cell-like representations, also reflecting compensatory activations.

Regressor	Parametric modulator	Temporal derivative modeled	Duration [seconds]
Regressors to model trial phases and response accuracy			
Cue	-	Yes	0
Retrieval		Yes	Variable
	Response accuracy[a]	Yes	Variable
Feedback	-	Yes	0
Re-encoding	-	Yes	Variable
Nuisance regressors			
Scanner drift	-	No	Session
Mean activation	-	No	Session
Head motion parameters	-	No	Session

[(a)] The parametric modulator contained equally distributed values of +2, +1, 0, -1, and -2.

REFERENCES

1. H. W. Querfurth, F. M. LaFerla, Alzheimer's disease. *N. Engl. J. Med.* **362**, 329–344 (2010). Medline doi:10.1056/NEJMra0909142

2. R. A. Sperling, C. R. Jack Jr., P. S. Aisen, Testing the right target and right drug at the right stage. *Sci. Transl. Med.* **3**, 111cm33 (2011). Medline

3. E. H. Corder, A. M. Saunders, W. J. Strittmatter, D. E. Schmechel, P. C. Gaskell, G. W. Small, A. D. Roses, J. L. Haines, M. A. Pericak-Vance, Gene dose of apolipoprotein E type 4 allele and the risk of Alzheimer's disease in late onset families. *Science* **261**, 921–923 (1993). Medline doi:10.1126/science.8346443

4. C. C. Liu, T. Kanekiyo, H. Xu, G. Bu, Apolipoprotein E and Alzheimer disease: Risk, mechanisms and therapy. *Nat. Rev. Neurol.* **9**, 106–118 (2013). Medline doi:10.1038/nrneurol.2012.263

5. H. Braak, E. Braak, Neuropathological stageing of Alzheimer-related changes. *Acta Neuropathol.* **82**, 239–259 (1991). Medline doi:10.1007/BF00308809

6. H. Braak, K. Del Tredici, The pathological process underlying Alzheimer's disease in individuals under thirty. *Acta Neuropathol.* **121**, 171–181 (2011). Medline doi:10.1007/s00401-010-0789-4

7. E. Ghebremedhin, C. Schultz, E. Braak, H. Braak, High frequency of apolipoprotein E ε4 allele in young individuals with very mild Alzheimer's disease-related neurofibrillary changes. *Exp. Neurol.* **153**, 152–155 (1998). Medline doi:10.1006/exnr.1998.6860

8. T. Hafting, M. Fyhn, S. Molden, M. B. Moser, E. I. Moser, Microstructure of a spatial map in the entorhinal cortex. *Nature* **436**, 801–806 (2005). Medline doi:10.1038/nature03721

9. J. Jacobs, C. T. Weidemann, J. F. Miller, A. Solway, J. F. Burke, X. X. Wei, N. Suthana, M. R. Sperling, A. D. Sharan, I. Fried, M. J. Kahana, Direct recordings of grid-like neuronal activity in human spatial navigation. *Nat. Neurosci.* **16**, 1188–1190 (2013). Medline doi:10.1038/nn.3466

10. G. Buzsáki, E. I. Moser, Memory, navigation and theta rhythm in the hippocampal-entorhinal system. *Nat. Neurosci.* **16**, 130–138 (2013). Medline doi:10.1038/nn.3304

11. M. E. Hasselmo, M. P. Brandon, Linking cellular mechanisms to behavior: Entorhinal persistent spiking and membrane potential oscillations may underlie path integration, grid cell firing, and episodic memory. *Neural Plast.* **2008**, 658323 (2008). Medline doi:10.1155/2008/658323

12. S. Sreenivasan, I. Fiete, Grid cells generate an analog error-correcting code for singularly precise neural computation. *Nat. Neurosci.* **14**, 1330–1337 (2011). Medline doi:10.1038/nn.2901

13. D. Bush, C. Barry, N. Burgess, What do grid cells contribute to place cell firing? *Trends Neurosci.* **37**, 136–145 (2014). Medline doi:10.1016/j.tins.2013.12.003

14. A. D. Ekstrom, M. J. Kahana, J. B. Caplan, T. A. Fields, E. A. Isham, E. L. Newman, I. Fried, Cellular networks underlying human spatial navigation. *Nature* **425**, 184–188 (2003). Medline doi:10.1038/nature01964

15. C. F. Doeller, C. Barry, N. Burgess, Evidence for grid cells in a human memory network. *Nature* **463**, 657–661 (2010). Medline doi:10.1038/nature08704

16. Materials and methods are available as supplementary materials on *Science* Online.

17. F. Berteau-Pavy, B. Park, J. Raber, Effects of sex and *APOE* ε4 on object recognition and spatial navigation in the elderly. *Neuroscience* **147**, 6–17 (2007). Medline doi:10.1016/j.neuroscience.2007.03.005

18. M. J. Chadwick, A. E. Jolly, D. P. Amos, D. Hassabis, H. J. Spiers, A goal direction signal in the human entorhinal/subicular region. *Curr. Biol.* **25**, 87–92 (2015). Medline doi:10.1016/j.cub.2014.11.001

19. S. Y. Bookheimer, M. H. Strojwas, M. S. Cohen, A. M. Saunders, M. A. Pericak-Vance, J. C. Mazziotta, G. W. Small, Patterns of brain activation in people at risk for Alzheimer's disease. *N. Engl. J. Med.* **343**, 450–456 (2000). Medline doi:10.1056/NEJM200008173430701

20. B. A. Strange, M. P. Witter, E. S. Lein, E. I. Moser, Functional organization of the hippocampal longitudinal axis. *Nat. Rev. Neurosci.* **15**, 655–669 (2014). Medline doi:10.1038/nrn3785

21. N. Filippini, B. J. MacIntosh, M. G. Hough, G. M. Goodwin, G. B. Frisoni, S. M. Smith, P. M. Matthews, C. F. Beckmann, C. E. Mackay, Distinct patterns of brain activity in young carriers of the *APOE*-ε4 allele. *Proc. Natl. Acad. Sci. U.S.A.* **106**, 7209–7214 (2009). Medline doi:10.1073/pnas.0811879106

22. M. S. Fanselow, H. W. Dong, Are the dorsal and ventral hippocampus functionally distinct structures? *Neuron* **65**, 7–19 (2010). Medline doi:10.1016/j.neuron.2009.11.031

23. A. Bakker, G. L. Krauss, M. S. Albert, C. L. Speck, L. R. Jones, C. E. Stark, M. A. Yassa, S. S. Bassett, A. L. Shelton, M. Gallagher, Reduction of hippocampal hyperactivity improves cognition in amnestic mild cognitive impairment. *Neuron* **74**, 467–474 (2012). Medline doi:10.1016/j.neuron.2012.03.023

24. A. W. Bero, P. Yan, J. H. Roh, J. R. Cirrito, F. R. Stewart, M. E. Raichle, J. M. Lee, D. M. Holtzman, Neuronal activity regulates the regional vulnerability to amyloid-β deposition. *Nat. Neurosci.* **14**, 750–756 (2011). Medline doi:10.1038/nn.2801

25. K. Hardcastle, S. Ganguli, L. M. Giocomo, Environmental boundaries as an error correction mechanism for grid cells. *Neuron* **86**, 827–839 (2015). Medline doi:10.1016/j.neuron.2015.03.039

26. L. Muessig, J. Hauser, T. J. Wills, F. Cacucci, A developmental switch in place cell accuracy coincides with grid cell maturation. *Neuron* **86**, 1167–1173 (2015). Medline doi:10.1016/j.neuron.2015.05.011

27. A. J. Trachtenberg, N. Filippini, C. E. Mackay, The effects of APOE-ε4 on the BOLD response. *Neurobiol. Aging* **33**, 323–334 (2012). Medline doi:10.1016/j.neurobiolaging.2010.03.009

28. C. F. Doeller, J. A. King, N. Burgess, Parallel striatal and hippocampal systems for landmarks and boundaries in spatial memory. *Proc. Natl. Acad. Sci. U.S.A.* **105**, 5915–5920 (2008). Medline doi:10.1073/pnas.0801489105

29. T. Wolbers, J. M. Wiener, H. A. Mallot, C. Büchel, Differential recruitment of the hippocampus, medial prefrontal cortex, and the human motion complex during path integration in humans. *J. Neurosci.* **27**, 9408–9416 (2007). Medline doi:10.1523/JNEUROSCI.2146-07.2007

30. K. R. Sherrill, U. M. Erdem, R. S. Ross, T. I. Brown, M. E. Hasselmo, C. E. Stern, Hippocampus and retrosplenial cortex combine path integration signals for successful navigation. *J. Neurosci.* **33**, 19304–19313 (2013). Medline doi:10.1523/JNEUROSCI.1825-13.2013

31. C. R. Mondadori, D. J. de Quervain, A. Buchmann, H. Mustovic, M. A. Wollmer, C. F. Schmidt, P. Boesiger, C. Hock, R. M. Nitsch, A. Papassotiropoulos, K. Henke, Better memory and neural efficiency in young apolipoprotein E ε4 carriers. *Cereb. Cortex* **17**, 1934–1947 (2007). Medline doi:10.1093/cercor/bhl103

32. F. Cacucci, M. Yi, T. J. Wills, P. Chapman, J. O'Keefe, Place cell firing correlates with memory deficits and amyloid plaque burden in Tg2576 Alzheimer mouse model. *Proc. Natl. Acad. Sci. U.S.A.* **105**, 7863–7868 (2008). Medline doi:10.1073/pnas.0802908105

33. T. Stöcker, T. Kellermann, F. Schneider, U. Habel, K. Amunts, P. Pieperhoff, K. Zilles, N. J. Shah, Dependence of amygdala activation on echo time: Results from olfactory fMRI experiments. *Neuroimage* **30**, 151–159 (2006). Medline doi:10.1016/j.neuroimage.2005.09.050

34. J. Ashburner, K. J. Friston, Unified segmentation. *Neuroimage* **26**, 839–851 (2005). Medline doi:10.1016/j.neuroimage.2005.02.018

35. A. M. Dale, B. Fischl, M. I. Sereno, Cortical surface-based analysis. I. Segmentation and surface reconstruction. *Neuroimage* **9**, 179–194 (1999). Medline doi:10.1006/nimg.1998.0395

36. B. Fischl, M. I. Sereno, A. M. Dale, Cortical surface-based analysis. II: Inflation, flattening, and a surface-based coordinate system. *Neuroimage* **9**, 195–207 (1999). Medline doi:10.1006/nimg.1998.0396

37. B. Fischl, A. M. Dale, Measuring the thickness of the human cerebral cortex from magnetic resonance images. *Proc. Natl. Acad. Sci. U.S.A.* **97**, 11050–11055 (2000). Medline doi:10.1073/pnas.200033797

38. B. Fischl, D. H. Salat, E. Busa, M. Albert, M. Dieterich, C. Haselgrove, A. van der Kouwe, R. Killiany, D. Kennedy, S. Klaveness, A. Montillo, N. Makris, B. Rosen, A. M. Dale, Whole brain segmentation: Automated labeling of neuroanatomical structures in the human brain. *Neuron* **33**, 341–355 (2002). Medline doi:10.1016/S0896-6273(02)00569-X

39. R. Insausti, K. Juottonen, H. Soininen, A. M. Insausti, K. Partanen, P. Vainio, M. P. Laakso, A. Pitkänen, MR volumetric analysis of the human entorhinal, perirhinal, and temporopolar cortices. *Am. J. Neuroradiol.* **19**, 659–671 (1998). Medline

40. C. Watson, F. Andermann, P. Gloor, M. Jones-Gotman, T. Peters, A. Evans, A. Olivier, D. Melanson, G. Leroux, Anatomic basis of amygdaloid and hippocampal volume measurement by magnetic resonance imaging. *Neurology* **42**, 1743–1750 (1992). Medline doi:10.1212/WNL.42.9.1743

41. E. A. Maguire, D. G. Gadian, I. S. Johnsrude, C. D. Good, J. Ashburner, R. S. Frackowiak, C. D. Frith, Navigation-related structural change in the hippocampi of taxi drivers. *Proc. Natl. Acad. Sci. U.S.A.* **97**, 4398–4403 (2000). Medline doi:10.1073/pnas.070039597

42. T. Hartley, E. A. Maguire, H. J. Spiers, N. Burgess, The well-worn route and the path less traveled: Distinct neural bases of route following and wayfinding in humans. *Neuron* **37**, 877–888 (2003). Medline doi:10.1016/S0896-6273(03)00095-3

43. M. Hirshhorn, C. Grady, R. S. Rosenbaum, G. Winocur, M. Moscovitch, Brain regions involved in the retrieval of spatial and episodic details associated with a familiar environment: An fMRI study. *Neuropsychologia* **50**, 3094–3106 (2012). Medline doi:10.1016/j.neuropsychologia.2012.08.008

44. L. Nadel, S. Hoscheidt, L. R. Ryan, Spatial cognition and the hippocampus: The anterior-posterior axis. *J. Cogn. Neurosci.* **25**, 22–28 (2013). Medline doi:10.1162/jocn_a_00313

45. D. M. Bannerman, R. Sprengel, D. J. Sanderson, S. B. McHugh, J. N. Rawlins, H. Monyer, P. H. Seeburg, Hippocampal synaptic plasticity, spatial memory and anxiety. *Nat. Rev. Neurosci.* **15**, 181–192 (2014). Medline doi:10.1038/nrn3677

46. P. Berens, CircStat: A Matlab toolbox for circular statistics. *J. Stat. Softw.* **31**, 10 (2009). doi:10.18637/jss.v031.i10

47. J. L. Woodard, S. T. Grafton, J. R. Votaw, R. C. Green, M. E. Dobraski, J. M. Hoffman, Compensatory recruitment of neural resources during overt rehearsal of word lists in Alzheimer's disease. *Neuropsychology* **12**, 491–504 (1998). Medline doi:10.1037/0894-4105.12.4.491

48. C. L. Grady, A. R. McIntosh, S. Beig, M. L. Keightley, H. Burian, S. E. Black, Evidence from functional neuroimaging of a compensatory prefrontal network in Alzheimer's disease. *J. Neurosci.* **23**, 986–993 (2003). Medline

49. M. W. Bondi, W. S. Houston, L. T. Eyler, G. G. Brown, fMRI evidence of compensatory mechanisms in older adults at genetic risk for Alzheimer disease. *Neurology* **64**, 501–508 (2005). Medline doi:10.1212/01.WNL.0000150885.00929.7E

50. C. Rosano, H. J. Aizenstein, J. L. Cochran, J. A. Saxton, S. T. De Kosky, A. B. Newman, L. H. Kuller, O. L. Lopez, C. S. Carter, Event-related functional magnetic resonance imaging investigation of executive control in very old individuals with mild cognitive impairment. *Biol. Psychiatry* **57**, 761–767 (2005). Medline doi:10.1016/j.biopsych.2004.12.031

51. S. D. Han, W. S. Houston, A. J. Jak, L. T. Eyler, B. J. Nagel, A. S. Fleisher, G. G. Brown, J. Corey-Bloom, D. P. Salmon, L. J. Thal, M. W. Bondi, Verbal paired-associate learning by APOE genotype in non-demented older adults: fMRI evidence of a right hemispheric compensatory response. *Neurobiol. Aging* **28**, 238–247 (2007). Medline doi:10.1016/j.neurobiolaging.2005.12.013

52. C. E. Wierenga, N. H. Stricker, A. McCauley, A. Simmons, A. J. Jak, Y. L. Chang, L. Delano-Wood, K. J. Bangen, D. P. Salmon, M. W. Bondi, Increased functional brain response during word retrieval in cognitively intact older adults at genetic risk for Alzheimer's disease. *Neuroimage* **51**, 1222–1233 (2010). Medline doi:10.1016/j.neuroimage.2010.03.021

53. N. A. Suthana, A. Krupa, M. Donix, A. Burggren, A. D. Ekstrom, M. Jones, L. M. Ercoli, K. J. Miller, P. Siddarth, G. W. Small, S. Y. Bookheimer, Reduced hippocampal CA2, CA3, and dentate gyrus activity in asymptomatic people at genetic risk for Alzheimer's disease. *Neuroimage* **53**, 1077–1084 (2010). Medline doi:10.1016/j.neuroimage.2009.12.014

54. C. R. Mondadori, A. Buchmann, H. Mustovic, C. F. Schmidt, P. Boesiger, R. M. Nitsch, C. Hock, J. Streffer, K. Henke, Enhanced brain activity may precede the diagnosis of Alzheimer's disease by 30 years. *Brain* **129**, 2908–2922 (2006). Medline doi:10.1093/brain/awl266

55. B. C. Dickerson, D. H. Salat, D. N. Greve, E. F. Chua, E. Rand-Giovannetti, D. M. Rentz, L. Bertram, K. Mullin, R. E. Tanzi, D. Blacker, M. S. Albert, R. A. Sperling, Increased hippocampal activation in mild cognitive impairment compared to normal aging and AD. *Neurology* **65**, 404–411 (2005). Medline doi:10.1212/01.wnl.0000171450.97464.49

56. K. A. Celone, V. D. Calhoun, B. C. Dickerson, A. Atri, E. F. Chua, S. L. Miller, K. DePeau, D. M. Rentz, D. J. Selkoe, D. Blacker, M. S. Albert, R. A. Sperling, Alterations in memory networks in mild cognitive impairment and Alzheimer's disease: An independent component analysis. *J. Neurosci.* **26**, 10222–10231 (2006). Medline doi:10.1523/JNEUROSCI.2250-06.2006

57. Y. T. Quiroz, A. E. Budson, K. Celone, A. Ruiz, R. Newmark, G. Castrillón, F. Lopera, C. E. Stern, Hippocampal hyperactivation in presymptomatic familial Alzheimer's disease. *Ann. Neurol.* **68**, 865–875 (2010). Medline doi:10.1002/ana.22105

58. D. Putcha, M. Brickhouse, K. O'Keefe, C. Sullivan, D. Rentz, G. Marshall, B. Dickerson, R. Sperling, Hippocampal hyperactivation associated with cortical thinning in Alzheimer's disease signature regions in non-demented elderly adults. *J. Neurosci.* **31**, 17680–17688 (2011). Medline doi:10.1523/JNEUROSCI.4740-11.2011

59. W. Huijbers, E. C. Mormino, A. P. Schultz, S. Wigman, A. M. Ward, M. Larvie, R. E. Amariglio, G. A. Marshall, D. M. Rentz, K. A. Johnson, R. A. Sperling, Amyloid-β deposition in mild cognitive impairment is associated with increased hippocampal activity, atrophy and clinical progression. *Brain* **138**, 1023–1035 (2015). Medline doi:10.1093/brain/awv007

60. W. J. Jagust, E. C. Mormino, Lifespan brain activity, β-amyloid, and Alzheimer's disease. *Trends Cogn. Sci.* **15**, 520–526 (2011). Medline doi:10.1016/j.tics.2011.09.004

61. C. F. Doeller, N. Burgess, Distinct error-correcting and incidental learning of location relative to landmarks and boundaries. *Proc. Natl. Acad. Sci. U.S.A.* **105**, 5909–5914 (2008). Medline doi:10.1073/pnas.0711433105

62. S. H. Yun, K. A. Park, P. Sullivan, J. F. Pasternak, M. J. Ladu, B. L. Trommer, Blockade of nicotinic acetylcholine receptors suppresses hippocampal long-term potentiation in wild-type but not ApoE4 targeted replacement mice. *J. Neurosci. Res.* **82**, 771–777 (2005). Medline doi:10.1002/jnr.20684